Geophysical Research Letters®

Key Points:

- Statistics of equatorial waves (EWs) differ markedly when using wavenumber-frequency filtering and spatial projection for wave identification
- Phase speed and variance of large-scale EWs are weakly dependent on resolution and convective treatment in ICON
- Mesoscale convective systems project onto westward inertio-gravity wave rainfall signatures without corresponding dynamical patterns

Supporting Information:

Supporting Information may be found in the online version of this article.

Correspondence to:

H. Jung,
hyunju.jung@kit.edu

Author Contributions:

Conceptualization: Hyunju Jung
Formal analysis: Hyunju Jung
Investigation: Hyunju Jung
Methodology: Hyunju Jung
Software: Hyunju Jung
Supervision: Peter Knippertz
Validation: Hyunju Jung, Peter Knippertz
Visualization: Hyunju Jung
Writing – original draft: Hyunju Jung
Writing – review & editing: Hyunju Jung, Peter Knippertz

Link Between the Time-Space Behavior of Rainfall and 3D Dynamical Structures of Equatorial Waves in Global Convection-Permitting Simulations

Hyunju Jung[1] and **Peter Knippertz[1]**

[1]Institute of Meteorology and Climate Research, Karlsruhe Institute of Technology, Karlsruhe, Germany

Abstract Equatorial waves (EWs) control a considerable portion of tropical rainfall variability but numerical models often struggle to capture them. Increased computing power now enables global simulations with resolved deep convection, which is believed to produce more realistic EWs. Here we identify EWs in global ICON simulations with varying horizontal resolution by (a) filtering rainfall based on space-time spectral analysis and (b) projecting wind and geopotential onto theoretical wave patterns. The simulations demonstrate that Kelvin, mixed-Rossby gravity and equatorial Rossby waves are consistently represented, regardless of model resolution and convective treatment. For smaller-scale inertio-gravity waves, however, explicit convection appears to be a prerequisite. Surprisingly, the associated rainfall signals are not accompanied by corresponding wind patterns but appear to be connected to mesoscale convective systems. This demonstrates the importance of analyzing rainfall and dynamical aspects of EWs jointly for a robust assessment.

Plain Language Summary Equatorial waves (EWs) are one of the most important weather features in the tropics. They propagate east- or westward, and substantially modulate rainfall on spatial scales from hundreds to ten thousands of kilometers and on temporal scales from a couple of days to several weeks. However, weather forecasting and climate models often fail to accurately capture them, and it is a challenge to objectively identify them in observational and model data. Here we investigate EWs in novel high-resolution global simulations, which represent the Earth's atmosphere as realistically as possible, by employing two different wave-identification methods, one that characterizes the time-space behavior of rainfall associated with waves and the other their spatial pattern in wind and pressure. Our results show that some types of EWs exhibit robust and realistic behaviors with little sensitivity to model configurations. However, small-scale wave types show significant propagating signals in rainfall but no corresponding wind patterns as we would expect from theory. We find that the time-space filter isolates large clusters of thunderstorms as small-scale waves, leading to a misinterpretation. Thus, a complementary analysis of wind pattern is required to objectively detect EWs.

1. Introduction

Equatorial waves (EWs) are zonally propagating disturbances trapped at the equator. They can couple with deep convection and thus control a considerable fraction of tropical rainfall variability (Kiladis et al., 2009; Takayabu, 1994; Yasunaga & Mapes, 2012). The most important types are Kelvin waves (KW hereafter), mixed-Rossby gravity waves (MRG), equatorial Rossby (ER) waves of the first meridional mode (ER) and west-ward inertio-gravity waves of the first meridional mode (WIG1). Mesoscale convective systems are generally associated with WIG1 (Nakazawa, 1988; Tulich & Kiladis, 2012), while synoptic-scale rainfall variability is often modulated by eastward propagating EWs (Roundy & Frank, 2004). From a practical point of view, convec-tively coupled EWs have potential for tropical rainfall predictions (Judt, 2020; Li & Stechmann, 2020; Ying & Zhang, 2017), which may also enhance midlatitude predictability (Dias & Kiladis, 2019; Pante & Knippertz, 2019; Scaife et al., 2017). EWs also interact with the Madden-Julian oscillation (Adames & Wallace, 2014; Zhang et al., 2020), which create implications for climate prediction (Lin et al., 2006).

Extracting the EW signal from observational or model data is a challenge (Knippertz et al., 2022; Žagar et al., 2022). In a recent methodological intercomparison study, Knippertz et al. (2022) found large discrepancies when comparing filtering methods based on narrow windows in wavenumber-frequency space and applied to precipitation and cloud fields from satellites and models, for example, Wheeler and Kiladis (1999, hereafter WK) with those relying mostly on a spatial projection of dynamical fields (horizontal wind and geopotential) onto theoretical patterns of EWs, for example, Yang et al. (2003, hereafter YP) and Žagar et al. (2009). YP identifies

EWs defined by solutions to the rotating, shallow-water equations on the equatorial β-plane (Matsuno, 1966) and thus does not require coupling of the EWs to precipitation and clouds. The method can be easily applied to short time windows of data and is thus suitable for real-time operational use (Yang et al., 2021). Due to the fundamental differences between the approaches, Knippertz et al. (2022) recommended using a combination of two different approaches to check for the robustness of the identified signals.

Weather and climate models still struggle to correctly represent EWs and convection parameterizations in the models are thought to be an important reason for that (Bengtsson et al., 2019; Dias et al., 2018; Lin et al., 2006). Advanced computing power is now allowing us to perform global high-resolution simulations with explicit representation of convection (Satoh et al., 2017; Stevens et al., 2019). This opens up new avenues for permitting multiscale interactions (Tomassini, 2020) and thus representing more realistic large-scale features such as convectively coupled EWs. Judt and Rios-Berrios (2021, hereafter JRB21) used the WK method applied to rainfall coarse-grained to a 2.5° grid in order to identify EWs in the Model for Prediction Across Scales-Atmosphere (MPAS-A) (Skamarock et al., 2012) from an intercomparison project of global convection-permitting models (DYAMOND) (Dynamics of the Atmospheric general circulation Modeled On Non-hydrostatic Domain; Stevens et al., 2019). They showed that it is explicit convection that improves rainfall variability associated with EWs rather than model resolution itself, in particular with respect to inertio-gravtiy waves, which MPAS hardly captures when using parameterized convection.

Going beyond JRB21, we address two important follow-up questions in this paper: (a) Are the conclusions of JRB21 with respect to model resolution and convective treatment robust for different model formulations? (b) Are the signals found in filtered rainfall accompanied by consistent dynamical structures, giving us confidence that they are "true" EWs (see discussion in Knippertz et al., 2022)? To answer the first question, we compare the results of JRB21 with corresponding analyses based on simulations using the ICON model (Icosahedral Nonhydrostatic Weather and Climate Model; Zängl et al., 2015) from DYAMOND. Although both models employ the mass flux convective scheme developed by Tiedtke (1989), MPAS uses a scale-aware form, where horizontal resolution determines how much convection is resolved (Wang, 2022), while ICON can represent convection either explicitly or through the parameterization. To answer the second question, we employ both the WK and YP methods to characterize EWs in the ICON simulations and use wave compositing techniques to relate results from the two approaches to each other.

2. Data and Methods

We use nine different global simulations conducted with the ICON model version 2.1.02. The configuration follows the DYAMOND protocol (Stevens et al., 2019). The simulations cover the period of 01 August–10 September 2016 and are initialized from the operational analyses of the European Centre for Medium-Range Weather Forecasts (ECMWF) on the first day at 00UTC. Sea surface temperatures and sea ice cover are prescribed using the ECMWF daily analysis. A detailed description of the model and experimental setup can be found in Hohenegger et al. (2020).

The ICON experiments have horizontal grid spacings of 2.5, 5, 10, 20, 40, and 80 km. Deep and shallow convection parameterizations (Bechtold et al., 2008; Tiedtke, 1989) are experimentally turned off for all six resolutions. For the three grid spacings between 20 and 80 km additional runs are conducted with parameterized deep and shallow convection.

To compare the experiments to observations, we use the globally gridded rainfall product Integrated Multi-Satellite Retrievals for Global Precipitation Measurement (GPM) (IMERG; Hou et al., 2014; Huffman et al., 2015), and dynamical and thermodynamical fields from the ERA5 reanalysis data set (Hersbach et al., 2020). Horizontal winds and geopotential at 200 hPa are used for the YP approach, and 3D horizontal winds and temperature on model levels for composite analyses. We interpolate model output and observational data to the same 1° lat-lon grid, which can better represent mesoscale convective structures than the 2.5° grid used by JRB21. ERA5 data are instantaneous fields every 6 hr and we use rainfall accumulation over the past 6-hr from IMERG (00, 06, 12, and 18UTC). This creates a small mismatch in time with ERA5, which given the time scales of EWs, should not have a large impact on our results. For simplicity, we refer to the IMERG and ERA5 data as observations.

Two EW identification methods are employed: WK, which filters rainfall based on narrow wavenumber-frequency windows for each wave type and YP, which projects horizontal wind and geopotential fields at 200 hPa onto

theoretical wave solutions. The former characterizes waves coupled to convection, while the latter identifies the waves' dynamical signatures that can be caused by dry or moist processes. The 200-hPa fields show reduced wave-convection coupling compared to the 850-hPa counterparts (not shown). Since the 40-day integration is rather short for the WK method, we adopt the technique used in Janiga et al. (2018, see their Figure 2), such that the 40-day model data are padded with two-year rainfall from IMERG beforehand and zeroes afterward. This deviates from JRB21, who applied a simple zero padding after the simulation period only. Sensitivity tests have shown that the finer 1° interpolation grid and different data-padding method somewhat reduce rainfall variance caused by EWs but this should not affect the conclusions from this work. For the analyses of rainfall (filtered and unfiltered) we regard averages over 5–15°N, where the rainfall maximum occurs during the simulation period in late boreal summer (Stevens et al., 2019). YP separates east- and westward moving components in a broad window of wavenumber and frequency before spatial projection. Here, we use wavenumbers 1–15 for all EWs as in Knippertz et al. (2022). For wave period we use 1.25–2.5 days for WIG1 and 3–30 days for the slower EWs (see Figure 2 in Yang et al., 2003). The meridional scale is set to 6° as in YP. Instead of a latitudinal average, each wave type can be characterized by a characteristic latitude, where the variance of the fixed pattern is large (Yang et al., 2021). Here we use u at 0° for KW, v at 0° for MRG, v at 8°N for ER and u at 0° for WIG1, respectively. Tropical depression (TD) such as easterly waves are prominent in the northern hemisphere during boreal summer. Since TDs have no eigenmodes, YP cannot identify them but WK detects them through their characteristic wavenumber and phase speed. (TDs are shown in Figure S1 in Supporting Information S1 for reference).

A composite technique is used to link EWs detected by the two approaches. Rainfall is composited on the basis of the YP wave-filtered dynamical structures and 3D dynamical and thermodynamical structures are composited on the basis of the WK wave-filtered rainfall. For YP two dynamical variables in quadrature to each other are selected to characterize the wave propagation as in Yang et al. (2021): du/dx and u at 0° for KW, v at 0° and u at 10°N for MRG, v at 8° and u at 0° for ER, and v at 10°N and u at 0° for WIG1. For WK, normalized fields of filtered rainfall and its tendency are used as in Schlueter et al. (2019), Yasunaga and Mapes (2012), and Riley et al. (2011). The composites are then based for both cases on eight characteristic phases, with Phase 5 indicating maximum rainfall in WK and maximum divergence in YP.

3. Results

We first present and discuss results for unfiltered rainfall, followed by analyses of KW, MRG, ER, and WIG1 for model grid spacings of 2.5, 20, and 80 km as well as a comparison to JRB21. (The full spectrum of models and EWs is provided in Figures S1 and S2 in Supporting Information S1). The last part will discuss the wave composites.

3.1. Unfiltered Rainfall

Figure 1 illustrates different characteristic behaviors of unfiltered rainfall from IMERG and the ICON simulations. IMERG shows well defined propagating and stationary features with large dry gaps in between, leading to an average rainfall of 0.28 mm h^{-1} (Figure 1a). There are fast westward propagating features over Africa and the downstream Atlantic as well as the eastern Pacific and indications of slow propagation over the western Pacific and Maritime Continent. In the ICON simulations (Figures 1b–1j) rainfall is considerably more widespread, leading to an overestimation of averaged rainfall by 10%–30%. For explicit convection (Figures 1b–1g), the clear westward propagation over Africa and the downstream Atlantic is well captured. However, the coarsest runs (40–80 km) unrealistically sharpen these structures, possibly due to some kind of wave-CISK mechanism (Conditional Instability of the Second Kind; Charney & Eliassen, 1964; Houze Jr, 2004), leading to a large overestimation in mean rainfall and variance. Parameterized convection (Figures 1h–1j) favors rainfall over the Maritime Continent and Indian Ocean, with some indication for westward propagation. Mean rainfall and variance are relatively consistent across the parameterized runs with the latter only about half that observed.

JRB21 also found an overall overestimation of mean rainfall in MPAS and an underestimation of variance with a marked degradation for parameterized convection. A noticeable difference to ICON is that in MPAS all wave propagation is weakened when parameterized convection is used, indicating an overall lower sensitivity to resolution and convective treatment in ICON that we will analyze further in the following subsections.
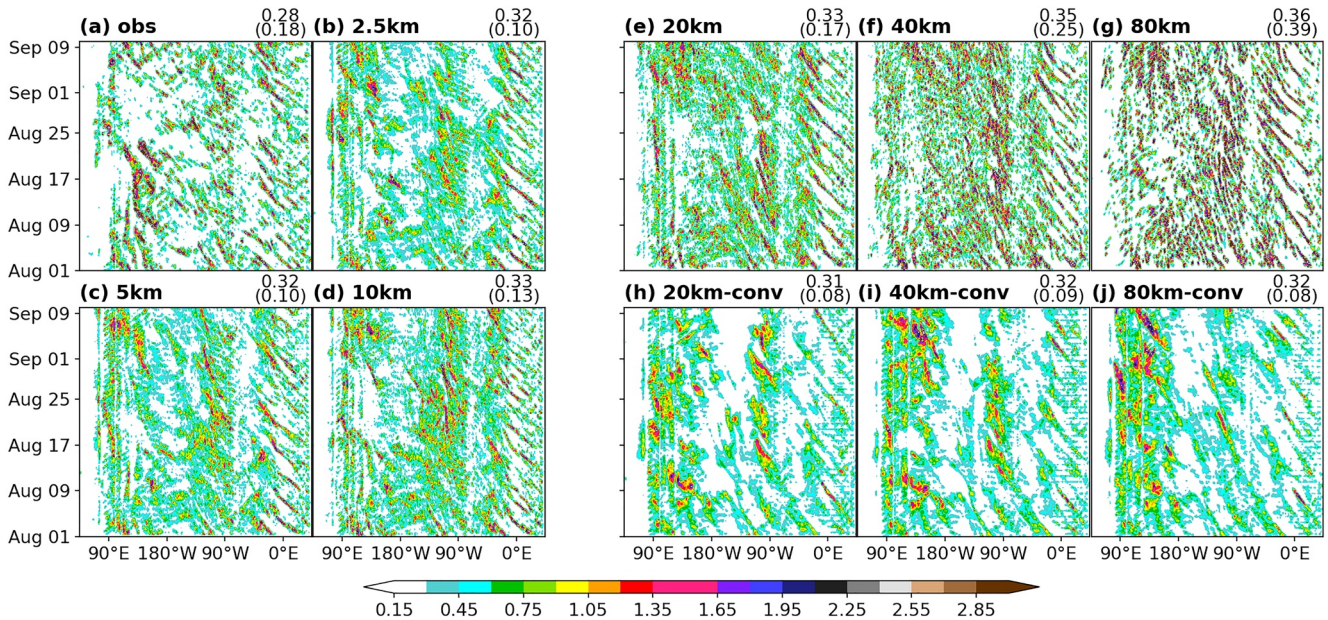
Figure 1. Hovmöller diagrams covering the period 01 August–10 September 2016 of unfiltered precipitation averaged over 5–15°N [mm h⁻¹] from IMERG satellite data (obs) and ICON model simulations. Bold numbers indicate the horizontal grid spacing of each run; conv marks the runs with parameterized convection. The numbers on the top right denote the mean precipitation averaged over the simulation period and latitudinal belt (5–15°N) [mm h⁻¹] and their variance in time and longitude [mm² h⁻²] are denoted in parenthesis. The color scheme is identical to JRB21 to facilitate comparison.

3.2. Kelvin Waves

Figure 2 shows a superposition of the results based on WK applied to rainfall and on YP using dynamical fields at 200 hPa for the different wave types, allowing for a qualitative comparison between the two methods. For a quantitative comparison, variance for each wave type and fraction of the total variance are shown in Figures S3 and S4 in Supporting Information S1. In Section 3.7, the WK and YP waves are linked by composite analyses. We begin with a discussion of KWs. In the observations (Figure 2a), several well developed KWs are discernible with propagation speeds of 10–12 m s⁻¹, particularly over the Pacific Ocean. Rainfall signals should be expected in areas of maximum upper-level divergence, and thus with easterlies shifted by a quarter wavelength to the west (and westerlies to the east, not shown). Rainfall activity in the central Pacific in late August is in fact accompanied by such anomalies but that is not true for all KWs identified from rainfall. One possible reason is that according to theory, KWs are symmetric about the equator with maximum zonal wind anomalies and divergence there. During our study period, rainfall maxima are shifted far into the northern hemisphere, which may lead to a general mismatch between the WK and YP results.

The corresponding ICON simulations (Figures 2b–2f) all show KW structures in rainfall with consistent phase speed (10–12 m s⁻¹) but with some—rather unsystematic—variation in intensity and geographical occurrence. Physically consistent phase relationships to zonal wind can be detected in the simulations, broadly similar to the observations. Occasionally, KW wind signals propagate faster than the signals in rainfall (e.g., in the 20-km run with parameterized convection), possibly indicating dry propagation with a larger equivalent depth. Rainfall variances of KW (Figure S3a in Supporting Information S1) are robust across the runs but underestimated relative to observations, except for the 80-km explicit run, while their wind variances are slightly overestimated (Figure S4a in Supporting Information S1). For both rain and wind, the fraction of the total variance is consistent with the observations (3%–4% for rainfall in Figure S3b in Supporting Information S1 and 6%–9% for wind in Figure S4b in Supporting Information S1). An exception is for rainfall variance when the horizontal grid is too coarse to explicitly represent deep convection ($\Delta x \geq 20$ km).

3.3. MRG Waves

In observations MRG-filtered rainfall signals propagate westward with a fast speed of 15–20 m s⁻¹ (Figure 2g). MRG activity is mostly restricted to the Indian and Pacific Oceans, and weakens in the course of the study period.
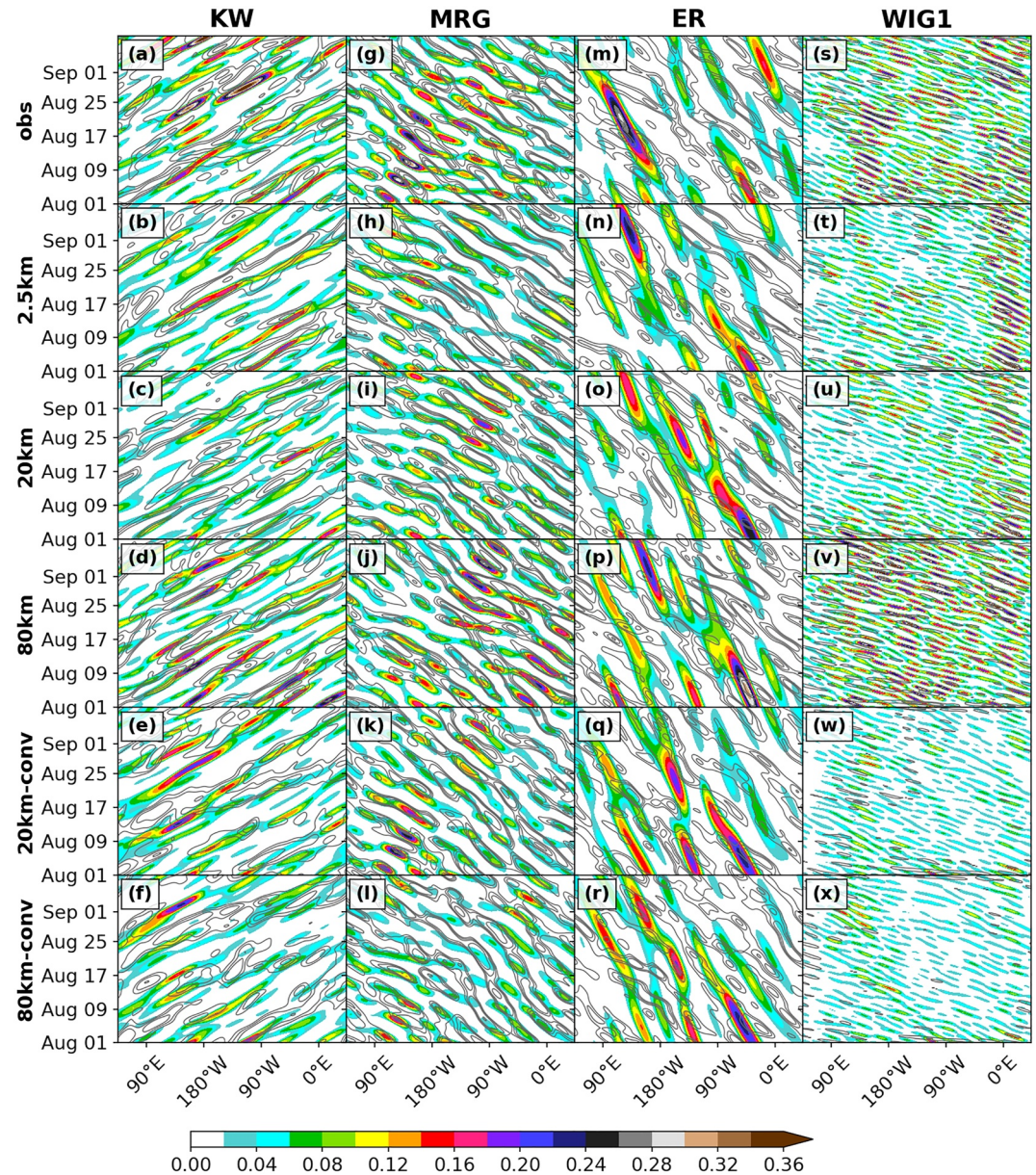
Figure 2. Hovmöller diagrams covering the period 01 August–10 September 2016 of filtered precipitation averaged over 5–15°N [mm h^{-1}] (shading) and filtered upper-level wind (contour) from IMERG satellite data and ERA5 (obs), respectively, as well as corresponding ICON model simulations. The contour lines show easterly wind anomalies for KW and WIG1 and northerly wind anomalies for mixed-Rossby gravity waves and ER, with contours of 1, 3, 5, and 10 m s^{-1}. Bold numbers indicate the horizontal grid spacing of each run; conv marks the runs with parameterized convection. The color scheme is identical to JRB21 to facilitate comparison.

There are also indications for a slow eastward group propagation consistent with MRG theory. MRG rainfall signals tend to move faster over the Pacific than Indian Ocean, which may be associated with a Doppler shift caused by the opposing low-level winds related to the Walker circulation (Takasuka et al., 2019). The theoretical structure of an MRG as used in YP implies that equatorial northerlies are accompanied by divergence at 10°N, favoring convection there. This is consistent with Figure 2g showing frequent overlap between northerly wind anomalies and enhanced rainfall in 5–15°N. The propagation speeds of MRG identified by the YP method are largely consistent with those by the WK method.

MRGs in the ICON runs (Figures 2h–2l) largely agree with those in the observations in terms of their phase speed and wind-rain relation, but there are also some considerable differences. The 20-km parameterized run matches

better with the observations than the 2.5-km run in terms of geographical locations of rainfall activity and fraction of the total rainfall variance (Figure S3b in Supporting Information S1). The other runs show various deviations from the observations, including an eastward shift of the activity (even all the way to Africa in the 80-km explicit run) and a mismatch of rain and wind propagation in the 80-km parameterized run. These differences demonstrate that high resolution and explicit convection are no simple cure to representing EWs and that it is the subtle coupling of dynamical and thermodynamical effects that need to be represented well in the model.

3.4. ER Waves

Figure 2m shows ER identified in observations by the two methods. Five significant signals in rainfall can be detected to propagate westward with a speed of 3–5 m s^{-1}, with an outstanding signal over the Indian Ocean in the middle of the investigation period. According to the ER spatial structure used in YP, meridional wind at 8°N coincides with divergence around this latitude and thus should favor convection. However, this relationship is hardly evident from Figure 2m, where the wind signals propagate much faster (10–12 m s^{-1}). This may be related to wave variability coupled to convection in WK and uncoupled in YP. Also, the Asian summer monsoon might influence the meridional structures of ER. Finally it is worth noting that the lower limit for wave periods is 6.25 days for WK and 3 days for YP, such that fast signals are suppressed by the WK filter.

Interestingly, the explicit runs (Figures 2n–2p) consistently show a very similar behavior, that is, marked individual events at almost all longitudes with a slow propagation in rainfall and a fast propagation in winds. In contrast, parameterized convection generally exhibits a closer alignment in propagation between wind and rainfall (Figures 2q–2r). Furthermore, ER significantly contributes to the total rainfall variance in the parameterized runs (5%–6%), even more than for the observations (2%) (Figure S3b in Supporting Information S1). This indicates that somehow parameterized convection responds more sensitively to the rotational (or balanced) flow of ERs than the more chaotic explicit convection (Raymond et al., 2015). Nevertheless, the results from the explicit runs closely match the observed variability and propagation speed.

3.5. WIG1 Waves

Finally for WIG1, the observations (Figure 2s) show strong and frequent rainfall signals over the Maritime Continent, downstream of Africa and occasionally elsewhere with 4% contribution to the total rainfall variance (Figure S3b in Supporting Information S1), while the corresponding u wind signals based on YP are very weak with 0.4% contribution (Figure S4b in Supporting Information S1). (WIG2 shows the same tendency of strong rainfall signals but weak wind signals, Figures S1–S4 in Supporting Information S1). This strongly suggests that the signals WK identifies do not show theoretical dynamical structures (further discussed in Section 3.7).

For WIG1, the ICON runs show a significant difference of rainfall signal between explicit and parameterized convection. For the former WIG1 contributes 2%–4% to the total rainfall variance and for the latter only 1% (Figure S3b in Supporting Information S1). Explicit runs with 2.5- and 20-km grid spacing show a strong activity over the African-Atlantic area but not over the Maritime Continent. The 80-km run with explicit convection has unrealistically strong signals at all longitudes, as already evident in the unfiltered rainfall. Moreover, in all ICON runs WIG1 hardly contributes to the total equatorial meridional wind variance (<1% in Figure S4b in Supporting Information S1). It is therefore questionable if WK isolates random small-scale features of rainfall as WIG1. We address this with composite analyses in Section 3.7.

3.6. Comparison to MPAS Results

The results described above have shown that the relationship between EWs, model resolution and convective treatment are complex in ICON. To first order, ICON consistently produces KW, MRG, and ER signals across all considered resolutions and convective treatments, despite underestimation of rainfall variance, and variations in geographical distribution and wind-rain relationship. An exception is the somewhat unrealistic 80-km run with explicit convection that produces large wave-related variance in rainfall but a low relative contribution by EWs. Only WIG1-filtered rainfall demonstrates a fundamental difference between explicit and parameterized runs with the latter showing very little activity overall. Again, the 80-km explicit run appears somewhat overdoing activity.

How does that relate to the results of JRB21? For KW, JRB21 found that convective parameterization slows down the propagation speed, which we do not observe for ICON. This means that to represent KW, MPAS benefits from

resolving convection, while little sensitivity is found in ICON. In MPAS, MRGs are consistent across different model configurations with some variations in variance, geographical maxima and propagation speed, broadly similar to our findings. For ER, JRB21 also found rather consistent results across all model configurations in close agreement with ICON. Finally WIG1 in ICON confirms a behavior shown in MPAS that associated rainfall signals are very weak with parameterized convection, while explicit convection emphasizes the activity over Africa and the Atlantic. (This geographical preference is also observed in tropical depression in both models, see Figure S1 in Supporting Information S1). Why the phase speed and variance of KW are more robust in ICON than in MPAS is unclear, as both in principle use a similar convection scheme (Tiedtke, 1989) but only the latter adapts the portion of parameterized convection depending on grid resolution (Wang, 2022). It is possible that couplings with other parameterizations or with the dynamical core create this difference but such links are hard to disentangle.
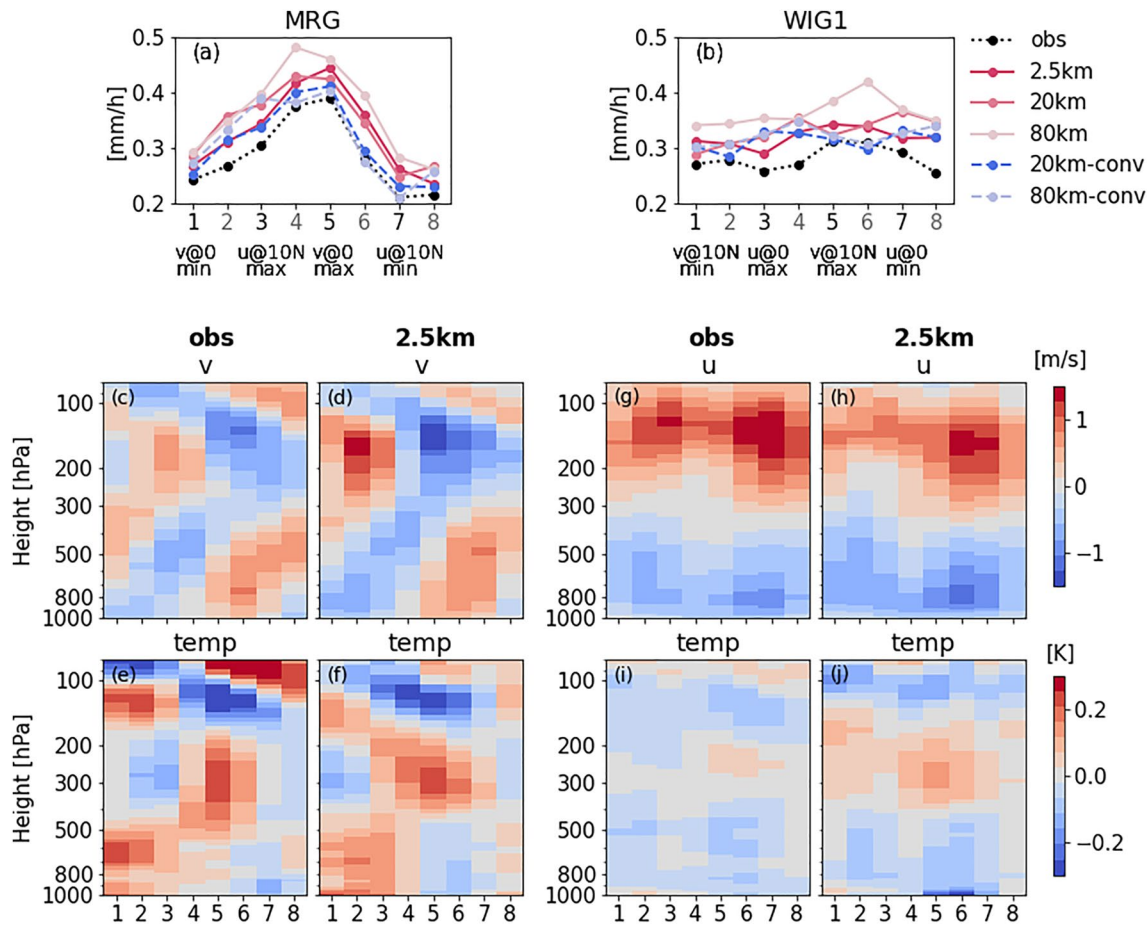
3.7. Composites

Figure 2 has revealed some striking differences between EWs detected using WK applied to rainfall and using YP applied to dynamical fields. Here we link the two methods using compositing techniques to shed some light into the structures of the identified signals. We concentrate on MRGs, for which we saw a good correspondence in Hovmöller diagrams, and WIG1 with very little wind signals overall. (The entire analyses can be found in Figures S5–S9 in Supporting Information S1).

Using the wind fields of YP as the basis, we can see a strong modulation of rainfall through MRGs (Figure 3a). The amplitude is similar across all configurations but shifted to higher values in ICON compared to IMERG. Maxima occur in Phase 5 (equatorial northerlies), as predicted by theory, in all runs but the two coarse-resolution explicit runs, where it occurs in Phase 4. This demonstrates that despite some subtle differences in the Hovmöller diagrams the mean relationships are robust. In strong contrast, the corresponding analysis for WIG1 (Figure 3b) shows no meaningful variation and inconsistencies between the model configurations, likely related to the overall weak wind signals.

When we take the opposite perspective and composite meteorological fields averaged over 5–15°N on the basis of wave phases from WK-filtered rainfall at the same latitudes, robust MRG structures become evident. For the wet Phase 5, northerly wind anomalies at 200 hPa are found (Figure 3c) as theory predicts. Wind structures then tilt toward lower phases below and above that level, forming an elbow structure. The corresponding analysis for temperature (Figure 3e) shows a baroclinic structure with warm anomalies in the lower troposphere before Phase 5 and at 300 hPa in Phase 5 with an opposite tilt in the lower stratosphere. These vertical structures resemble those described in other observational studies (Kiladis et al., 2009; Wheeler et al., 2000).

The vertical structures of wind and temperature from the 2.5-km run correspond well to those in the observations despite an underestimation of the lower-stratospheric temperature anomalies (Figures 3d and 3f). The other runs also exhibit realistic vertical structures (Figure S4 in Supporting Information S1), indicating that MRG-rainfall coupling is produced well by ICON, irrespective of convective treatment and wave-identification method.

For WIG1 both observations and the ICON model show a weak modulation of temperature and zonal wind with the wave phase based on WK-filtered rainfall (Figures 3g–3j). If WIG1 existed during the study period, the composite analyses would present some sinusoidal patterns as for MRG. An intriguing point is that the associated signals are not small but show a westerly anomaly at high levels and an easterly anomaly at low levels, while the temperature shows a trimodal structure (cold-warm-cold). Such structures are typical for African Easterly Waves (Kiladis et al., 2006), which are active during this time of year over the area where we find WIG1 (Figure 2). These environmental conditions are typical for the formation of westward moving mesoscale convective systems (MCSs), the rainfall signature of which then projects into the WIG1 wavenumber-frequency window without showing the corresponding dynamical structures. The modulations indeed are consistent with this interpretation. After the rainfall maximum in Phase 5, low-level easterlies increase, caused by downward momentum transport from the African easterly jet. Meanwhile, low-level cooling is caused by cold pools and midlevel heating by latent heat release in the stratiform part of the MCS. It is well known that models with parameterized convection struggle to realistically represent the complicated convective dynamics of MCSs (Marsham et al., 2013; Pante & Knippertz, 2019; Pantillon et al., 2015).

Figure 3. Composite of unfiltered rainfall on the basis of (a) mixed-Rossby gravity waves (MRG) and (b) WIG1 wave phase identified by the YP method. Composite of unfiltered horizontal wind and temperature anomalies on the basis of (c–f) MRG and (g–j) WIG1 wave phase identified by the WK method. Composited variables are averaged over 5–15°N.

4. Conclusions

Judt and Rios-Berrios (2021, JRB21) reported that resolved deep convection provides more realistic simulations of EWs, particularly the inertio-gravity type of waves, than parameterized deep convection in the MPAS simulations from DYAMOND (Stevens et al., 2019). Inspired by their work, we have characterized EWs in the corresponding ICON simulations by employing a combination of two different filtering approaches for a robust comparison of EWs: one based on a wavenumber-frequency method using rainfall (Wheeler & Kiladis, 1999, WK) and the other based on a spatial-projection method using upper-level wind and geopotential (Yang et al., 2003, YP).

The main conclusions are summarized as follows:

1. All ICON runs produce westward propagating features in unfiltered rainfall, broadly corresponding to observations. Compared to the observations, ICON produces more widespread rainfall patterns, leading to an overestimation of mean rainfall, which was also found for MPAS. Rainfall variance is underestimated for parameterized convection but overestimated for the experimental coarse-resolution explicit ICON runs ($\Delta x > 20$ km). A discernible distinction between the two models is that the westward propagation was suppressed for parameterized convection in MPAS (JRB21).

2. In the ICON model, Kelvin (KW), mixed-Rossby gravity (MRG) and equatorial Rossby (ER) waves are largely consistent in terms of propagation speed and variance, irrespective of resolution, convective treatment and wave-identification method. Wave-related variances in rainfall are generally underestimated but their contributions to the total rainfall variance is realistic, except for the explicit runs with coarse resolutions ($\Delta x \geq 20$ km). Variances in horizontal winds are consistent with the observations. Furthermore, we

demonstrate that MRG robustly modulates rainfall and vertical structures of winds and temperature. Our results of wave-filtered rainfall largely agree with JRB21 but KW phase speed is less sensitive to model configuration in ICON than MPAS.

3. Westward inertio-gravity waves (WIG1) exhibit a big difference between explicit and parameterized convection in both ICON and MPAS when using the WK approach. However, their wind signals (YP) are very feeble, irrespective of convective treatment, indicating no corresponding dynamical structure of WIG1. A composite analysis, which links the two approaches, reveals that this spurious signal is not a classical EW but likely signal from MCSs, amongst others associated with African Easterly Waves, which are in fact better represented with explicit convection, as previous studies have shown.

Given the limited simulation period available, the main conclusions presented here may not hold for other seasons, as each wave type has its own annual cycle (Wheeler et al., 2000). Slow-moving waves such as ER in particular might be different over a longer time integration. A new generation of convection-permitting climate models will become available for better sampling in the foreseeable future (Palmer & Stevens, 2019). Despite these caveats, our application of both the WK and YP tools ensures detected EWs from two complementary perspectives and helps avoid misinterpretation of signals from one method (see Knippertz et al., 2022, for a detailed discussion). The robustness of large-scale EWs to model configuration in ICON is encouraging. This bodes well for a successful use of ICON in different resolutions for weather and climate predictions in the future.

Data Availability Statement

IMERG data are available through the NASA earth data portal (https://doi.org/10.5067/GPM/IMERG/3B-HH/06). The ERA5 data on pressure levels can be found at the Copernicus Climate Change Service (C3S) Climate Data Store (https://doi.org/10.24381/cds.bd0915c6). The ERA5 data on model levels are accessible via Meteorological Archival and Retrieval System (MARS) (https://apps.ecmwf.int/data-catalogues/era5/?class=ea). DYAMOND data are archived by the German Climate Computing Center (DKRZ) and are accessible upon request from the ESiWACE project (https://www.esiwace.eu/services/dyamond-initiative).

References

Adames, Á. F., & Wallace, J. M. (2014). Three-dimensional structure and evolution of the MJO and its relation to the mean flow. *Journal of the Atmospheric Sciences*, *71*(6), 2007–2026. https://doi.org/10.1175/JAS-D-13-0254.1

Bechtold, P., Köhler, M., Jung, T., Doblas-Reyes, F., Leutbecher, M., Rodwell, M. J., et al. (2008). Advances in simulating atmospheric variability with the ECMWF model: From synoptic to decadal time-scales. *Quarterly Journal of the Royal Meteorological Society*, *134*(634), 1337–1351. https://doi.org/10.1002/qj.289

Bengtsson, L., Dias, J., Gehne, M., Bechtold, P., Whitaker, J., Bao, J.-W., et al. (2019). Convectively coupled equatorial wave simulations using the ECMWF IFS and the NOAA GFS cumulus convection schemes in the NOAA GFS model. *Monthly Weather Review*, *147*(11), 4005–4025. https://doi.org/10.1175/MWR-D-19-0195.1

Charney, J. G., & Eliassen, A. (1964). On the growth of the hurricane depression. *Journal of the Atmospheric Sciences*, 21(1), 68–75. https://doi.org/10.1175/1520-0469(1964)021⟨0068:OTGOTH⟩2.0.CO;2

Dias, J., Gehne, M., Kiladis, G. N., Sakaeda, N., Bechtold, P., & Haiden, T. (2018). Equatorial waves and the skill of NCEP and ECMWF numerical weather prediction systems. *Monthly Weather Review*, *146*(6), 1763–1784. https://doi.org/10.1175/mwr-d-17-0362.1

Dias, J., & Kiladis, G. N. (2019). The influence of tropical forecast errors on higher latitude predictions. *Geophysical Research Letters*, *46*(8), 4450–4459. https://doi.org/10.1029/2019GL082812

Hersbach, H., Bell, B., Berrisford, P., Hirahara, S., Horányi, A., Muñoz-Sabater, J., et al. (2020). The ERA5 global reanalysis. *Quarterly Journal of the Royal Meteorological Society*, *146*(730), 1999–2049. https://doi.org/10.1002/qj.3803

Hohenegger, C., Kornblueh, L., Klocke, D., Becker, T., Cioni, G., Engels, J. F., et al. (2020). Climate statistics in global simulations of the atmosphere, from 80 to 2.5 km grid spacing. *Journal of the Meteorological Society of Japan*, *98*(1), 73–91. https://doi.org/10.2151/jmsj.2020-005

Hou, A. Y., Kakar, R. K., Neeck, S., Azarbarzin, A. A., Kummerow, C. D., Kojima, M., et al. (2014). The global precipitation measurement mission. *Bulletin of the American Meteorological Society*, *95*(5), 701–722. https://doi.org/10.1175/BAMS-D-13-00164.1

Houze, R. A., Jr. (2004). Mesoscale convective systems. *Reviews of Geophysics*, *42*(4). https://doi.org/10.1029/2004RG000150

Huffman, G. J., Bolvin, D. T., Braithwaite, D., Hsu, K., Joyce, R., Xie, P., & Yoo, S.-H. (2015). NASA global precipitation measurement (GPM) integrated multi-satellite retrievals for GPM (IMERG). *Algorithm Theoretical Basis Document (ATBD) Version*, *4*(26), 30. Retrieved from http://pmm.nasa.gov/sites/default/files/document_files/IMERG_ATBD_V4.5.pdf

Janiga, M. A., Schreck, C., III., Ridout, J. A., Flatau, M., Barton, N. P., Metzger, E. J., & Reynolds, C. A. (2018). Subseasonal forecasts of convectively coupled equatorial waves and the MJO: Activity and predictive skill. *Monthly Weather Review*, *146*(8), 2337–2360. https://doi.org/10.1175/MWR-D-17-0261.1

Judt, F. (2020). Atmospheric predictability of the tropics, middle latitudes, and polar regions explored through global storm–resolving simulations. *Journal of the Atmospheric Sciences*, *77*(1), 257–276. https://doi.org/10.1175/JAS-D-19-0116.1

Judt, F., & Rios-Berrios, R. (2021). Resolved convection improves the representation of equatorial waves and tropical rainfall variability in a global nonhydrostatic model. *Geophysical Research Letters*, *48*(14), e2021GL093265. https://doi.org/10.1029/2021GL093265

Kiladis, G. N., Thorncroft, C. D., & Hall, N. M. (2006). Three-dimensional structure and dynamics of African easterly waves. Part I: Observations. *Journal of the Atmospheric Sciences*, *63*(9), 2212–2230. https://doi.org/10.1175/JAS3741.1

Kiladis, G. N., Wheeler, M. C., Haertel, P. T., Straub, K. H., & Roundy, P. E. (2009). Convectively coupled equatorial waves. *Reviews of Geophysics*, *47*(2), RG2003. https://doi.org/10.1029/2008RG000266

Knippertz, P., Gehne, M., Kiladis, G. N., Kikuchi, K., Rasheeda Satheesh, A., Roundy, P. E., et al. (2022). The intricacies of identifying equatorial waves. *Quarterly Journal of the Royal Meteorological Society*, *148*(747), 2814–2852. https://doi.org/10.1002/qj.4338

Li, Y., & Stechmann, S. N. (2020). Predictability of tropical rainfall and waves: Estimates from observational data. *Quarterly Journal of the Royal Meteorological Society*, *146*(729), 1668–1684. https://doi.org/10.1002/qj.3759

Lin, J.-L., Kiladis, G. N., Mapes, B. E., Weickmann, K. M., Sperber, K. R., Lin, W., et al. (2006). Tropical intraseasonal variability in 14 IPCC AR4 climate models. Part I: Convective signals. *Journal of Climate*, *19*(12), 2665–2690. https://doi.org/10.1175/JCLI3735.1

Marsham, J. H., Dixon, N. S., Garcia-Carreras, L., Lister, G. M., Parker, D. J., Knippertz, P., & Birch, C. E. (2013). The role of moist convection in the West African monsoon system: Insights from continental–scale convection–permitting simulations. *Geophysical Research Letters*, *40*(9), 1843–1849. https://doi.org/10.1002/grl.50347

Matsuno, T. (1966). Quasi-geostrophic motions in the equatorial area. *Journal of the Meteorological Society of Japa*n, *44*(1), 25–43. https://doi.org/10.2151/jmsj1965.44.1_25

Nakazawa, T. (1988). Tropical super clusters within intraseasonal variations over the western Pacific. *Journal of the Meteorological Society of Japan*, *66*(6), 823–839. https://doi.org/10.2151/jmsj1965.66.6_823

Palmer, T., & Stevens, B. (2019). The scientific challenge of understanding and estimating climate change. *Proceedings of the National Academy of Sciences of the United States of America*, *116*(49), 24390–24395. https://doi.org/10.1073/pnas.1906691116

Pante, G., & Knippertz, P. (2019). Resolving Sahelian thunderstorms improves mid-latitude weather forecasts. *Nature Communications*, *10*(1), 3487. https://doi.org/10.1038/s41467-019-11081-4

Pantillon, F., Knippertz, P., Marsham, J. H., & Birch, C. E. (2015). A parameterization of convective dust storms for models with mass–flux convection schemes. *Journal of the Atmospheric Sciences*, *72*(6), 2545–2561. https://doi.org/10.1175/JAS-D-14-0341.1

Raymond, D., Fuchs, Ž., Gjorgjievska, S., & Sessions, S. (2015). Balanced dynamics and convection in the tropical troposphere. *Journal of Advances in Modeling Earth Systems*, *7*(3), 1093–1116. https://doi.org/10.1002/2015MS000467

Riley, E. M., Mapes, B. E., & Tulich, S. N. (2011). Clouds associated with the Madden–Julian oscillation: A new perspective from CloudSat. *Journal of the Atmospheric Sciences*, *68*(12), 3032–3051. https://doi.org/10.1175/JAS-D-11-030.1

Roundy, P. E., & Frank, W. M. (2004). A climatology of waves in the equatorial region. *Journal of the Atmospheric Sciences*, *61*(17), 2105–2132. https://doi.org/10.1175/1520-0469(2004)061⟨2105:ACOWIT⟩2.0.CO;2

Satoh, M., Tomita, H., Yashiro, H., Kajikawa, Y., Miyamoto, Y., Yamaura, T., et al. (2017). Outcomes and challenges of global high-resolution non-hydrostatic atmospheric simulations using the K computer. *Progress in Earth and Planetary Scienc*e, *4*(13), 1–24. https://doi.org/10.1186/s40645-017-0127-8

Scaife, A. A., Comer, R. E., Dunstone, N. J., Knight, J. R., Smith, D. M., MacLachlan, C., et al. (2017). Tropical rainfall, Rossby waves and regional winter climate predictions. *Quarterly Journal of the Royal Meteorological Society*, *143*(702), 1–11. https://doi.org/10.1002/qj.2910

Schlueter, A., Fink, A. H., Knippertz, P., & Vogel, P. (2019). A systematic comparison of tropical waves over northern Africa. Part I: Influence on rainfall. *Journal of Climate*, *32*(5), 1501–1523. https://doi.org/10.1175/JCLI-D-18-0173.1

Skamarock, W. C., Klemp, J. B., Duda, M. G., Fowler, L. D., Park, S.-H., & Ringler, T. D. (2012). A multiscale nonhydrostatic atmospheric model using centroidal Voronoi tesselations and C-grid staggering. *Monthly Weather Review*, *140*(9), 3090–3105. https://doi.org/10.1175/MWR-D-11-00215.1

Stevens, B., Satoh, M., Auger, L., Biercamp, J., Bretherton, C. S., Chen, X., et al. (2019). DYAMOND: The DYnamics of the Atmospheric general circulation Modeled On Non-hydrostatic Domains. *Progress in Earth and Planetary Science*, *6*(1), 61. https://doi.org/10.1186/s40645-019-0304-z

Takasuka, D., Satoh, M., & Yokoi, S. (2019). Observational evidence of mixed Rossby-gravity waves as a driving force for the MJO convective initiation and propagation. *Geophysical Research Letters*, *46*(10), 5546–5555. https://doi.org/10.1029/2019GL083108

Takayabu, Y. N. (1994). Large-scale cloud disturbances associated with equatorial waves Part I: Spectral features of the cloud disturbances. *Journal of the Meteorological Society of Japan*, *72*(3), 433–449. https://doi.org/10.2151/jmsj1965.72.3_433

Tiedtke, M. (1989). A comprehensive mass flux scheme for cumulus parameterization in large-scale models. *Monthly Weather Review*, *117*(8), 1779–1800. https://doi.org/10.1175/1520-0493(1989)117⟨1779:ACMFSF⟩2.0.CO;2

Tomassini, L. (2020). The interaction between moist convection and the atmospheric circulation in the tropics. *Bulletin of the American Meteorological Society*, *101*(8), E1378–E1396. https://doi.org/10.1175/BAMS-D-19-0180.1

Tulich, S. N., & Kiladis, G. N. (2012). Squall lines and convectively coupled gravity waves in the tropics: Why do most cloud systems propagate westward? *Journal of the Atmospheric Sciences*, *69*(10), 2995–3012. https://doi.org/10.1175/JAS-D-11-0297.1

Wang, W. (2022). Forecasting convection with a "scale-aware" Tiedtke cumulus parameterization scheme at kilometer scales. *Weather and Forecasting*, *37*(8), 1491–1507. https://doi.org/10.1175/WAF-D-21-0179.1

Wheeler, M., & Kiladis, G. N. (1999). Convectively coupled equatorial waves: Analysis of clouds and temperature in the wavenumber–frequency domain. *Journal of the Atmospheric Sciences*, *56*(3), 374–399. https://doi.org/10.1175/1520-0469(1999)056⟨0374:CCEWAO⟩2.0.CO;2

Wheeler, M., Kiladis, G. N., & Webster, P. J. (2000). Large-scale dynamical fields associated with convectively coupled equatorial waves. *Journal of the Atmospheric Sciences*, *57*(5), 613–640. https://doi.org/10.1175/1520-0469(2000)057⟨0613:LSDFAW⟩2.0.CO;2

Yang, G.-Y., Ferrett, S., Woolnough, S., Methven, J., & Holloway, C. (2021). Real-time identification of equatorial waves and evaluation of waves in global forecasts. *Weather and Forecasting*, *36*(1), 171–193. https://doi.org/10.1175/WAF-D-20-0144.1

Yang, G.-Y., Hoskins, B., & Slingo, J. (2003). Convectively coupled equatorial waves: A new methodology for identifying wave structures in observational data. *Journal of the Atmospheric Sciences*, *60*(14), 1637–1654. https://doi.org/10.1175/1520-0469(2003)060⟨1637:CCEWAN⟩2.0.CO;2

Yasunaga, K., & Mapes, B. (2012). Differences between more divergent and more rotational types of convectively coupled equatorial waves. Part II: Composite analysis based on space–time filtering. *Journal of the Atmospheric Sciences*, *69*(1), 17–34. https://doi.org/10.1175/JAS-D-11-034.1

Ying, Y., & Zhang, F. (2017). Practical and intrinsic predictability of multiscale weather and convectively coupled equatorial waves during the active phase of an MJO. *Journal of the Atmospheric Sciences*, *74*(11), 3771–3785. https://doi.org/10.1175/JAS-D-17-0157.1

Žagar, N., Lunkeit, F., Sielmann, F., & Xiao, W. (2022). Three-dimensional structure of the equatorial Kelvin wave: Vertical structure functions, equivalent depths, and frequency and wavenumber spectra. *Journal of Climate*, *35*(7), 2209–2230. https://doi.org/10.1175/JCLI-D-21-0342.1

Žagar, N., Tribbia, J., Anderson, J., & Raeder, K. (2009). Uncertainties of estimates of inertia–gravity energy in the atmosphere. Part II: Large-scale equatorial waves. *Monthly Weather Review*, *137*(11), 3858–3873. https://doi.org/10.1175/2009MWR2816.1

Zängl, G., Reinert, D., Rípodas, P., & Baldauf, M. (2015). The ICON (ICOsahedral Non–hydrostatic) modelling framework of DWD and MPI–M: Description of the non–hydrostatic dynamical core. *Quarterly Journal of the Royal Meteorological Society*, *141*(687), 563–579. https://doi.org/10.1002/qj.2378

Zhang, C., Adames, Á., Khouider, B., Wang, B., & Yang, D. (2020). Four theories of the Madden-Julian oscillation. *Reviews of Geophysics*, *58*(3), e2019RG000685. https://doi.org/10.1029/2019RG000685